

SigVLP: Sigmoid Volume-Language Pre-Training for Self-Supervised CT-Volume Adaptive Representation Learning

Jiayi Wang¹ Hadrien Reynaud¹ Ibrahim Ethem Hamamci^{2,3,4} Sezgin Er^{2,4}
 Suprosanna Shit^{2,3} Bjoern Menze^{2,3} Bernhard Kainz^{5,1}

¹Friedrich-Alexander University Erlangen-Nürnberg, Germany

²Department of Quantitative Biomedicine, University of Zurich, Switzerland

³ETH AI Center, ETH Zurich, Switzerland

⁴International School of Medicine, Istanbul Medipol University, Turkey

⁵Department of Computing, Imperial College London, UK

{jiayi.w.wang, hadrien.reynaud}@fau.de

{ibrahim.hamamci, bjoern.menze, suprosanna.shit}@uzh.ch

sezgin.er@std.medipol.edu.tr b.kainz@imperial.ac.uk

Abstract

Large-scale, volumetric medical imaging datasets typically aggregate scans from different vendors and devices, resulting in highly variable resolution, slice thicknesses, and numbers of slices per study. Consequently, training representation models usually requires cropping or interpolating along the z-axis to obtain fixed-size blocks, which inevitably causes information loss. We propose a new training approach to overcome this limitation. Instead of absolute position embeddings, we interpret volumes as sequences of 3D chunks and adopt Rotary Position Embeddings, allowing us to treat the z-axis as an unconstrained temporal dimensions. Building on this idea, we introduce a new vision-language model: SigVLP. In SigVLP, we implement Rotary Position Embedding as the positional encoding method, which is applied directly within the attention operation, generating input-conditioned sine and cosine weights on the fly. This design ensures consistent alignment between query and key projections and adapts to any input sizes. To allow for variable input size during training, we sample Computed Tomography volumes in chunks and pair them with localized organ-wise textual observations. Compared to using entire reports for conditioning, chunkwise alignment provides finer-grained supervision, enabling the model to establish stronger correlations between the text and volume representations, thereby improving the precision of text-to-volume alignment. Our models are trained with the Muon optimizer and evaluated on a diverse set of downstream tasks, including zero-shot abnormality and or-

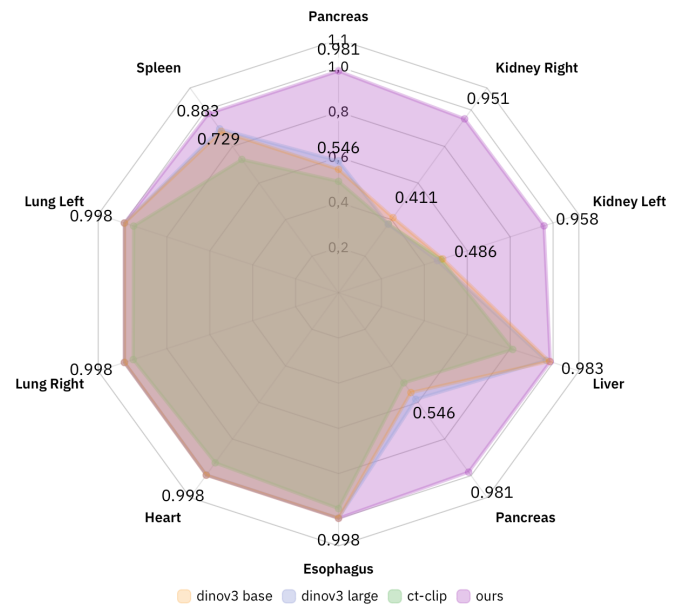


Figure 1. Radar chart of average Precision for organ presence classification using Linear Probes: comparison between SigVLP (ours), CT-Clip and DINOv3 variants (Base, Large) with identical linear probe structures.

gan classification, segmentation, and retrieval tasks.

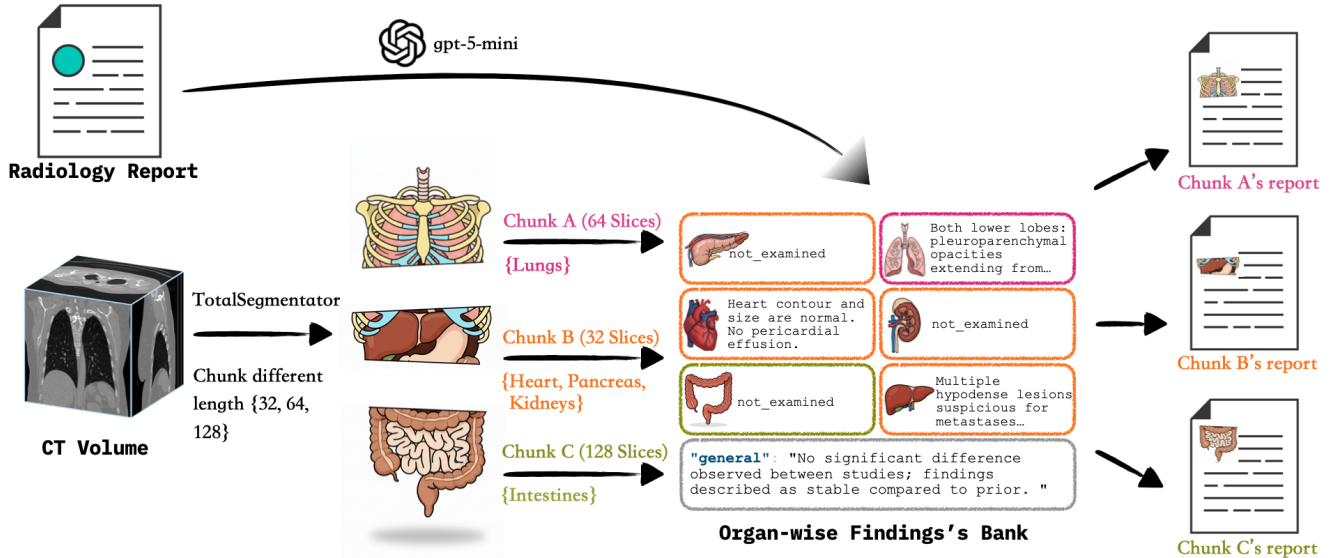


Figure 2. Our approach for Organ-wise Radiology Report Generation: The original CT volume is segmented into organ masks [47, 53]. The volume is then split into blocks of different lengths, where the masks indicate which organs should be included for report generation. Organ-specific findings are extracted with GPT-5 mini to construct an organ findings bank, stored as individual entries. A general description is appended to summarize the entire volume.

1. Introduction

Strong universal embeddings are the foundation of modern Vision-Language Models (VLMs) such as CLIP [34], enabling semantic alignment between visual and textual domains. In the natural image domain, such models have transformed downstream learning by allowing general-purpose representations that can be leveraged across diverse tasks [24, 25], ranging from object detection to image captioning, alleviating the need for expensive training operations. Translating this success to medical imaging, however, remains an open challenge.

Recent medical adaptations such as ConVIRT [57], CT-CLIP [15, 16] and MedCLIP [46] have attempted to replicate this paradigm for clinical data. Yet, these models are limited by both the scale and structure of available training data and compute scale. For example, CT-CLIP is primarily trained on chest CT data, leading to narrow representation spaces that fail to generalize across modalities, organs, and institutions. Similarly, vision-language pretraining on datasets such as MIMIC-CXR [20] captures only 2D chest radiographs with short, templated reports, offering limited representation depth for complex 3D anatomy. As a result, embeddings from these models often encode local visual or textual cues rather than holistic, cross-anatomical semantics that are essential for volumetric reasoning. An alternative line of work avoids full 3D processing by selecting a few representative slices, which improves efficiency at the cost of spatial completeness [45]. Additionally, early 3D medi-

cal VLM attempts that enforce multi-view consistency still struggle to preserve true volumetric coherence [28].

Nevertheless, most of these methods for volumetric medical image analysis relies heavily on large-scale datasets. However, due to strict privacy regulations, fully open-access and standardized datasets remain scarce. For instance, CT-RATE [13] offers over 40,000 full volumetric 3D CT scans, in comparison to MIMIC-CXR, which includes nearly 377,000 chest radiographs from more than 65,000 patients, but only in 2D. Although both datasets are widely used in computer vision research, they also illustrate a fundamental challenge: heterogeneity in data representation. Nonetheless, CT-RATE provides complete 3D volumes, whereas MIMIC-CXR includes only cropped (single or dual) 2D views.

In addition to limited medical data, another core obstacle in medical imaging lies in the lack of cross-institutional standardization. Scans from different vendors and devices often differ significantly in XY spacing, rescale intercept, rescale slope, particularly along the z-axis (slice-wise direction in 3D volumes). While normalization methods such as interpolation or cropping can be applied, they systematically lead to data loss. Additionally, most scanners will output fixed-size x-y slices, while the z-axis is much more variable due to patient size and slice thickness. This limitation is significant when transferring pretrained models from large-scale datasets to organ-specific tasks, such as kidney tumor segmentation (KiTS) [18], liver tumor segmentation (LiTS) [4], or brain tumor segmentation (BraTS) [3].

Recent 3D VLMs exemplify this issue by resampling every study to a fixed 3D grid to match architectural constraints [1, 52]. While it simplifies batching and training, this process leads to the loss of clinically relevant details.

On the contrary to the need to accommodate variable slices, most methods are limited by reliance on fixed slice numbers. Such restriction is often enforced due to architectural constraints in Transformer-based models [17], especially when using absolute positional embeddings [22]. These embeddings typically require a fixed-length token sequence, whether for visual or textual input, a limitation that becomes problematic when handling 3D volumes with varying slice counts. In contrast, Rotary Positional Encoding (RoPE) [38] has shown strong potential in handling sequence variability in video-based Transformers, where it effectively encodes temporal relationships without requiring fixed-length inputs. A concurrent direction addresses variable depth by first encoding 2D slices and then aggregating them with a dedicated Z-former, which reduces memory yet reconstructs 3D context only post hoc [23]. Our approach maintains within-chunk spatio-temporal structure directly in the volumetric encoder.

Motivated by advancements in video representation learning, particularly from works like CTFLOW [43] and EchoFlow [35], we treat 3D medical volumes as sequences of 3D chunks, analogous to video frames, but extended to 3D. In this setting, Rotary Positional Embeddings are useful, as they assign each token a unique rotationally-invariant positional signature. Rather than using fixed positional indices, RoPE captures relative dependencies across tokens through a rotation matrix applied to query-key projections, enabling better long-range context modeling. This mechanism is particularly powerful in long-sequence modeling tasks, and has been widely adopted in Large Language Models (LLMs) such as LLaMA [40], Qwen [2], and Kimi-K2 [39]. While 1D RoPE suffices for long textual sequences, volumetric settings require 3D positional schemes [31]. To address this, various RoPE extensions, like VideoRoPE [49] VideoRoPE++ [48], TAD-RoPE [11] and M-RoPE [44] have been developed to better model spatial layouts and temporal continuity in 2D and 3D data.

Building upon these insights, we propose a dynamic, chunk-wise training pipeline that eliminates the fixed-length constraint along the z -axis. Instead of aligning the entire visual volume with full-length textual reports, we introduce a fine-grained, region-specific alignment strategy using enhanced, re-structured reports. Our approach extends the SigLIPv2 architecture [41], which builds on a pairwise sigmoid objective shown to stabilize large-scale vision-language pretraining [55].

To account for variations in scan lengths, we train the model on 3D chunks, where the total number of slices varies between 32, 64, and 128. We leverage the state-

of-the-art Muon optimizer [21, 30] to facilitate stable and efficient learning across variable-length inputs. Drawing inspiration from the organ-wise alignment strategies [36], we segment entire volumes into smaller anatomical blocks. Correspondingly, we crop the original radiology report into organ-specific segments to ensure meaningful alignment between text and visual chunks.

For this, we first use a lightweight language model (GPT-5-mini) to decompose radiology reports organ-wise. Next, anatomical segmentation masks, generated by [47, 53], allow us to accurately determine the anatomical contents of each chunk and match it to the corresponding report fragment. We then reconstruct reports, based on the content of each sampled chunk on the fly.

We evaluate our embedding space on downstream tasks such as *zero-shot abnormality classification* and *disease diagnosis*, which are standard benchmarks for assessing vision-language alignment. Experimental results show that our method significantly improves performance across these tasks. In summary, our contributions are:

- **On-the-fly subvolume-observations alignment.** We design a train-time method to allow retrieval of relevant clinical observations for the organs present in any sampled subvolume, allowing optimal alignment of our text and volume encoders outputs.
- **Large-scale volumetric vision-language pretraining.** We advance volumetric foundation modeling by pretraining SigVLP on a large publicly available corpus of 3D CT volumes (CT-RATE), demonstrating for the first time that anatomically consistent vision-language alignment can emerge at scale. SigVLP unifies spatial continuity and semantic abstraction through adopted ideas from Large Language models, such as RoPe [48, 49] and Muon [21].
- **Organ-wise clinical observations dataset.** We release an open-source dataset of organ-wise clinical observations, automatically extracted from free-text radiology reports using a custom LLM-assisted text analysis approach, on top of the publicly available CT-RATE dataset.
- **Downstream performance improvements.** We explore the expressivity of our learned representations by evaluating our embeddings on a wide range of downstream tasks, demonstrating the benefits of our approach.

2. Related Works

Recent advances in medical vision-language pretraining (Med-VLP) have mainly targeted 2D chest X-rays (CXR), using contrastive learning to align images with reports [6, 42, 54, 57]. While effective, such global alignment overlooks fine-grained associations between image regions and report segments [7]. To enrich textual representation, Med-CLIP [50] and KAD [56] embed domain knowledge, and Imitate [29] applies hierarchical alignment between visual and structured text features. MedCLIP [46] and PTUni-

fier [9] train on unpaired corpora, while PairAug [51] expands supervision through synthetic pairing.

Med-VLP has since extended to 3D imaging, particularly CT [5, 13, 36, 58]. VELVET-Med [58] and CT-CLIP [13] align CT volumes with radiology reports, and Merlin [5] integrates structured electronic health records data for abdomen-level modeling. To overcome the spatial rigidity of fixed-grid inputs, T3D [28] introduces a multi-view 3D CLIP but lacks volumetric continuity. DC-Former [1] and Med3DVLM [52] decompose volumes hierarchically yet still resample scans to uniform grids; the latter also employs a pairwise sigmoid contrastive loss [55], validating its effectiveness. MS-VLM [23] aggregates 2D slice features via a Z-former to support variable-length scans but reconstructs 3D context only post-hoc. Our framework instead preserves volumetric coherence through dynamic chunk-wise processing rather than slice aggregation or fixed decomposition.

Some works pursue fine-grained, organ-level alignment. CT-GLIP [26] builds organ-level image-text pairs to localize structures and align each with text reports. fVLM [36] similarly performs anatomy-level contrastive learning for detailed CT understanding. These methods show the utility of localized supervision but collapse scans into pooled organ features, losing z-axis continuity. Our approach retains volumetric context by aligning variable-length subvolumes with relevant report segments, enabling dynamic RoPE-based modeling without resampling.

Recent grounding-oriented works explore partial supervision and multi-modal weak labels: MedFinder [8] aligns CT sub-regions with report phrases for retrieval, and PET/CT grounding [19] fuses modalities at fine granularity. These demonstrate growing interest in spatially grounded medical VLPs, though they rely on curated landmarks or multi-stage training.

3. Method

Preprocessing. We convert each full free-text report from the CT-RATE dataset to an organ-indexed dictionary using a lightweight LLM. After evaluating GPT 5 [33], GPT 5 Mini [33], GPT 5 Nano [33], DeepSeek R1 [12] and Qwen 1.5B [2], we selected GPT 5 Mini because it yielded the best cost-quality trade-off. For each organ $o \in \mathcal{O}$ the record $\text{Findings}(o) = (s_o, f_o)$ with $s_o \in \{\text{normal}, \text{abnormal}, \text{not_examined}\}$ and free-text $f_o \in \Sigma_{\text{alnum}}$. An optional global note is $g = \text{Findings}(\text{general})$. We enforce $s_o = \text{not_examined} \Rightarrow f_o = \text{"not_examined"}$. During training, given a 4D organ mask $\mathbf{M} \in \{0, 1\}^{T \times H \times W \times |\mathcal{O}|}$, we sample chunks with length $\ell \sim \mathcal{U}(\{32, 64, 128\})$ and starting z-axis slice $s \sim \mathcal{U}(\{0, \dots, T - \ell\})$. We define $\mathcal{C} = \{s, \dots, s + \ell - 1\}$, and retrieve organs present in the

chunks such that

$$\mathcal{O}_{\mathcal{C}} = \{o \in \mathcal{O} \mid \max_{t \in \mathcal{C}, x, y} \mathbf{M}(t, x, y, o) = 1\}.$$

Train-time Chunk Composition. If $\mathcal{O}_{\mathcal{C}} = \emptyset$, we return “No target structures were detected in this CT block.” Otherwise, we partition the organs by status

$$\begin{aligned} \mathcal{A} &= \{o \in \mathcal{O}_{\mathcal{C}} : s_o = \text{abnormal}, f_o \neq \emptyset\}, \\ \mathcal{N} &= \{o \in \mathcal{O}_{\mathcal{C}} : s_o = \text{normal}, f_o \neq \emptyset\}, \\ \mathcal{X} &= \{o \in \mathcal{O}_{\mathcal{C}} : s_o = \text{not_examined}\}. \end{aligned}$$

Let the $\text{Join}(\cdot)$ operation generate a coma-separated list and \oplus denote the whitespace concatenation. We compose

$$\begin{aligned} S_{\mathcal{X}} &= (\text{List}(\mathcal{X}) + \text{"were not examined."}) \mathbf{1}[\lvert \mathcal{X} \rvert > 0], \\ S_{\mathcal{N}} &= \text{Join}(\{f_o\}_{o \in \mathcal{N}}), \\ S_{\mathcal{A}} &= \text{Join}(\{f_o\}_{o \in \mathcal{A}}), \\ S_g &= g \cdot \mathbf{1}[g \notin \{\emptyset, \text{"not_examined"}\}]. \end{aligned}$$

The final description $D(\mathcal{C}) = S_{\mathcal{X}} \oplus S_{\mathcal{N}} \oplus S_{\mathcal{A}} \oplus S_g$ yields organ-aware, chunk-aligned supervision at multiple “temporal” scales $\ell \in \{32, 64, 128\}$. This chunk-wise approach is effective for volumetric vision-language learning: rather than aligning a single global report to an entire scan, we establish fine-grained, spatially localized correspondences between subvolumes and their relevant textual findings. Overlapping chunks ensure anatomical continuity across boundaries and mitigate label leakage, while fixed-length subvolumes normalize variable scan depths and enable dynamic batching. Thus, each 3D CT scan is composed of dozens of well-grounded supervision pairs, increasing the density and quality of learning signals. It allows us to capture both global and local anatomical semantics, learn position-aware embeddings without resampling, and achieve improved generalization across heterogeneous imaging protocols.

Rotary Position Embedding. To support variable-length volumes, we remove additive absolute positional embeddings and apply RoPE directly inside the attention operation. Let the hidden states be $\mathbf{H} \in \mathbb{R}^{B \times L \times C}$ with B batch size, L sequence length, and C channels. We compute projections

$$\mathbf{Q} = \mathbf{H}\mathbf{W}^Q, \quad \mathbf{K} = \mathbf{H}\mathbf{W}^K, \quad \mathbf{V} = \mathbf{H}\mathbf{W}^V, \quad (1)$$

and reshape to $B \times H \times L \times d$ with H heads and $d = C/H$.

For position $t \in \{0, \dots, L - 1\}$ and paired index $r \in \{0, \dots, \frac{d}{2} - 1\}$, we define a geometric frequency with base $b > 1$:

$$\omega_r = b^{-\frac{2r}{d}}, \quad \theta_{t,r} = t\omega_r, \quad (2)$$

and we use RoPE base $b = 1000$. We write a head’s query $\mathbf{q}_t \in \mathbb{R}^d$ as a pair $(q_{t,r}^{(0)}, q_{t,r}^{(1)})$ (even/odd dimensions). RoPE

rotates each pair:

$$\tilde{q}_{t,r}^{(0)} = q_{t,r}^{(0)} \cos \theta_{t,r} - q_{t,r}^{(1)} \sin \theta_{t,r}, \quad (3)$$

$$\tilde{q}_{t,r}^{(1)} = q_{t,r}^{(0)} \sin \theta_{t,r} + q_{t,r}^{(1)} \cos \theta_{t,r}, \quad (4)$$

and analogously for keys to obtain $\tilde{\mathbf{k}}_t$. Values are left unchanged. Stacking all pairs yields $\tilde{\mathbf{Q}}, \tilde{\mathbf{K}} \in \mathbb{R}^{B \times H \times L \times d}$.

Attention. We compute the scaled dot-product attention with an additive mask \mathbf{M} :

$$\mathbf{A} = \text{softmax} \left(\frac{\tilde{\mathbf{Q}} \tilde{\mathbf{K}}^\top}{\sqrt{d}} + \mathbf{M} \right), \quad (5)$$

$$\mathbf{O} = \mathbf{A} \mathbf{V}; \mathbf{O}_{\text{proj}} = \text{Concat}_{h=1}^H (\mathbf{O}_h) \mathbf{W}_O, \quad (6)$$

where $\mathbf{O}_h \in \mathbb{R}^{B \times L \times d}$ is the output of head h , H is the total number of heads, and $\mathbf{W}_O \in \mathbb{R}^{(Hd) \times C}$ is the standard output projection matrix that linearly combines all heads and maps the concatenated attention output back to the model dimension C . In this implementation, RoPE is applied to \mathbf{Q}/\mathbf{K} only, computed on-the-fly from the current L , thus enabling dynamic sequence lengths with no additional parameters and negligible overhead.

4. Experiments

We use the **CT-RATE** [14] dataset for all our experiments, using 40k+ CT volumes for training and a fully isolated 3k+ set for validation (no patient overlap). Training was done on 16 nodes, with $4 \times \text{H100}$ GPUs per node and a per-GPU batch size of 8, giving a global batch of $B_{\text{global}} = 8 \times 4 \times 16 = 512$. We use a learning rate of 1×10^{-3} and weight decay 1×10^{-4} . To reduce inter-scanner variation, all slices are resized in-plane to 256×256 . Text supervision uses the dataset-provided, volume-associated radiology reports; anatomy grounding uses high-confidence masks from [47].

Our downstream tasks include zero-shot abnormality classification using whole-chunk representations to assess CLIP-style text-vision alignment, linear-probe classification and segmentation on frozen embeddings to measure anatomical precision and the separability of organ-specific features, as well as chunk-wise organ presence classification. We also evaluate text-image retrieval, which directly assess localized visual-textual correspondence and the effectiveness of our on-the-fly chunk-text alignment pretraining strategy. Our primary emphasis is on the vision component: we test whether a chunk-wise training strategy enables fine-grained, detail-level alignment. We compare CT-specific variants, CT-CLIP (baseline), CT-Vocab (vocabulary fine-tuned), and CT-LiPro (classification fine-tuned), and include DINOv3-base [10, 37] as a standalone, general-purpose visual backbone to gauge out-of-domain generalization. Fig. 3 presents eight UMAP [32] embedding projection plots: CT-CLIP [13], CT-Vocab [13], CT-LiPro [14],

DINOv3-base [37], and our model at four different training stages. In each plot, similar hues correspond to semantically similar labels. We observe that DINOv3 produces separated clusters while most CT-specific baselines exhibit few isolated clusters. During training, after around 500 optimization steps, both training loss and validation metrics stabilize, yet representation structure continues to evolve as the training progresses. At 2,000 steps (Fig. 3(e)), the projection already shows clear color separation, resembling the fine-tuned CT-LiPro. At 234,930 steps, our embeddings are projected as a continuous and uniform hue, indicating that the model has learned a smooth, structured representation of the underlying feature space. We interrupted training at 234,930 ($\approx 120\text{M}$ examples seen) as scaling laws tells us that at that stage, only order of magnitudes more training would impact the quality of the model.

Table 1. Retrieval performance between 200-slice 3D CT volumes and corresponding radiology reports. The baseline uses the initial **SigLIP2** weights released in [41]. For our proposed **SigVLP** method, we employ reconstructed reports generated through our pipeline. At each evaluation step, 100 samples are retrieved from a total of 1,500 candidates, and all recall values are computed based on the top-100 retrieval results.

Model	R@5 \uparrow	R@10 \uparrow	R@50 \uparrow	MeanRank \downarrow
SigLIPv2-L [41]	0.047 \pm 0.007	0.101 \pm 0.009	0.504 \pm 0.011	50.53 \pm 0.39
CT-Clip [13]	0.204 \pm 0.038	0.348 \pm 0.052	0.835 \pm 0.049	26.01 \pm 3.01
CT-Vocab [13]	0.055 \pm 0.012	0.107 \pm 0.015	0.517 \pm 0.013	49.12 \pm 0.80
Dinov3-Clip [10]	0.047 \pm 0.020	0.107 \pm 0.027	0.501 \pm 0.024	50.53 \pm 1.06
Ours	0.636 \pm 0.050	0.769 \pm 0.036	0.978 \pm 0.010	8.23 \pm 0.947

Retrieval Performance between 3D Volume and Radiology Report. In Table 1, we present the retrieval performance of different CLIP variants, including CT-specific CLIPs and general 2D image CLIPs such as DINOv3-CLIP and our baseline SigLIP2. For the 2D models, we averaged slice-level features, and used them as input, but these models performed poorly, indicating their limited ability to capture meaningful medical information. However, 3D models like CT-CLIP achieved higher results, indicating that it could retrieve valid matches. Our SigVLP demonstrates a significant and statistically valid improvement over all previous methods, with a MeanRank of 8.23 ± 0.947 compared to the CT-Clip’s 26.01 ± 3.01 .

Whole-Body Abnormality Classification and Organ-Wise Segmentation. Our downstream results reveal a clear scale-dependent trade-off in the learned features. In the linear-probe classification experiments in Table 2, DINOv3 attains near-perfect recall of 0.996 but only 0.21 precision, which indicates features that are highly sensitive yet weakly selective. Our final model achieves the best precision of 0.435 and the highest accuracy of 0.80, which reflects a clean separation of true positives from hard negatives.

The linear-probe segmentation, performed in a down-sampled patch-level space and reported in Table 2 (Seg-

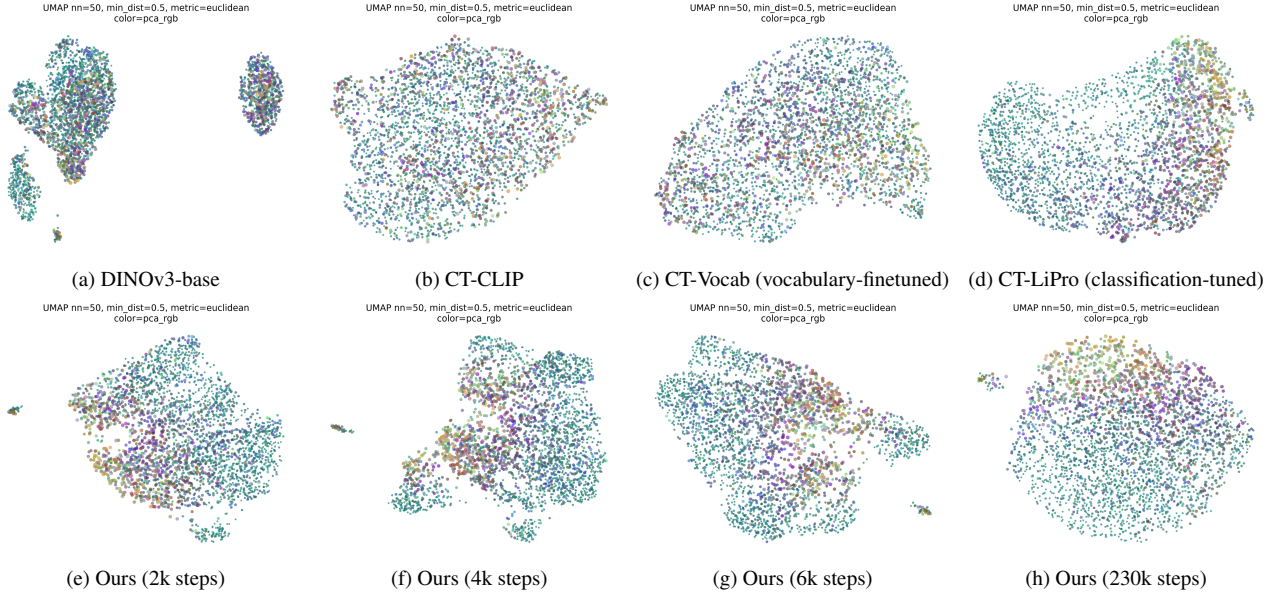


Figure 3. **UMAP [32] visualization of evaluation embeddings** across baselines and our model. Colors indicate abnormality classes, with similar hues corresponding to semantically related labels. *Top row*: DINOv3-base, CT-CLIP, CT-Vocab (vocabulary-finetuned), CT-LiPro (classification-finetuned). *Bottom row*: Our method at 2k, 4k, 6k, and 234,930 training steps.

Table 2. Classification: linear classification on 18 abnormalities. Segmentation: linear MLP segmentation, where Segmentation (Dice) shows the results for three representative organs, and Segmentation (Overall) shows mDice and mIoU over 12 organs. For both classification and segmentation, performance is summarized using per-organ mean values and standard deviations. Classification results report standard deviations obtained via bootstrap sampling. Segmentation results report standard deviations across 12 organs. Zero values indicate that no valid mask was produced (all background label), not missing entries.

Backbone	Classification					Segmentation (Dice)			Segmentation (Overall)	
	Precision	Recall	F1	Accuracy	AUROC	Task01 (lung_left)	Task02 (Aorta)	Task03 (Stomach)	mDice	mIoU
SigLIPv2-L [41]	0.362±0.041	0.518±0.038	0.388±0.028	0.756±0.013	0.706±0.028	0.000	0.000	0.000	0.000±0.000	0.000±0.000
CT-CLIP [13]	0.288±0.065	0.424±0.044	0.305±0.048	0.764±0.016	0.639±0.031	0.105	0.000	0.000	0.013±0.029	0.007±0.015
CT-Vocab [13]	0.300±0.060	0.463±0.031	0.333±0.036	0.765±0.019	0.653±0.042	0.005	0.000	0.000	0.000±0.000	0.000±0.000
DINOv3-S [37]	0.330±0.025	0.815 ±0.032	0.455 ±0.029	0.516±0.011	0.651±0.023	0.816	0.002	0.237	0.292±0.257	0.226±0.201
DINOv3-B [37]	0.332±0.032	0.712±0.052	0.437±0.036	0.553±0.019	0.649±0.031	0.876	0.278	0.340	0.448±0.289	0.362±0.251
DINOv3-L [37]	0.342±0.022	0.714±0.032	0.446±0.022	0.569±0.014	0.654±0.033	0.849	0.117	0.199	0.316±0.305	0.250±0.240
Ours (2000 step)	0.355±0.020	0.632±0.029	0.418±0.016	0.702±0.020	0.709 ±0.024	0.794	0.376	0.255	0.374±0.261	0.287±0.215
Ours (4000 step)	0.408±0.042	0.551±0.032	0.429±0.034	0.727±0.008	0.708±0.024	0.800	0.318	0.346	0.392±0.300	0.304±0.255
Ours (230000 step)	0.429 ±0.034	0.428±0.028	0.410±0.028	0.778 ±0.013	0.683±0.016	0.786	0.471	0.489	0.487 ±0.253	0.381 ±0.203

mentation (Dice) and (Overall)), further exposes the impact of object scale. DINOv3 performs better on large organs where coarse cues suffice. For medium and small structures such as the aorta or the stomach, our chunk-aligned volumetric features’ expressivity surpass DINOv3’s. On the aorta, the Dice score improves from 0.278 to 0.471, a 1.7× improvement. Our model achieves the best mean Dice, supporting the conclusion that it captures finer anatomical details from volumetric data.

Qualitative comparisons in Fig. 4 echo these trend. DINOv3 covers a large fraction of pixels on large organs such as the lung and the spleen, which yields broad coverage but

less precise boundaries. Our model produces tighter masks on smaller structures such as the stomach, and the predicted contours follow the ground truth more closely. DINOv3 is attractive for exhaustive screening where high recall is the priority, whereas our features are preferable for precise delineation and margin-sensitive decisions. These results demonstrate, again, that the embeddings produced by our model retain much more information for small structures while retaining large-scale structure information.

Chunk-Wise and Organ-Wise Linear-Probe Classification and Free-Form Retrieval. During training, we chunk each volume into blocks and generate masks and reports at

Table 3. Comparison of classification (linear probe) and zero-shot retrieval performance across different slice numbers. The upper part shows 12-organ presence binary classification, where the reported standard deviations are organ-wise. The lower part presents zero-shot retrieval performance, with standard deviations obtained via bootstrap sampling (subset size = 50 samples per bootstrap iteration).

Classification (Linear Probe)															
Method	32 slices					64 slices					128 slices				
	Precision	Recall	F1	AUC	mAP	Precision	Recall	F1	AUC	mAP	Precision	Recall	F1	AUC	mAP
SigLIPv2-L [41]	0.499 \pm 0.399	0.494 \pm 0.491	0.496 \pm 0.367	0.523 \pm 0.251	0.542 \pm 0.345	0.599 \pm 0.393	0.614 \pm 0.397	0.607 \pm 0.332	0.630 \pm 0.215	0.592 \pm 0.364	0.665 \pm 0.349	0.767 \pm 0.380	0.712 \pm 0.381	0.652 \pm 0.189	0.705 \pm 0.334
CT-CLIP [13]	0.792 \pm 0.396	0.668 \pm 0.491	0.725 \pm 0.440	0.840 \pm 0.076	0.661 \pm 0.204	0.832 \pm 0.427	0.745 \pm 0.300	0.786 \pm 0.435	0.879 \pm 0.100	0.696 \pm 0.288	0.851 \pm 0.421	0.871 \pm 0.471	0.861 \pm 0.437	0.895 \pm 0.075	0.699 \pm 0.288
CT-Vocab [13]	0.819 \pm 0.360	0.661 \pm 0.467	0.731 \pm 0.420	0.850 \pm 0.060	0.668 \pm 0.187	0.937 \pm 0.441	0.711 \pm 0.495	0.809 \pm 0.481	0.894 \pm 0.106	0.682 \pm 0.306	0.851 \pm 0.421	0.871 \pm 0.471	0.861 \pm 0.437	0.877 \pm 0.081	0.671 \pm 0.299
Dinov3-S [37]	0.982 \pm 0.436	0.919 \pm 0.458	0.950 \pm 0.446	0.990 \pm 0.120	0.517 \pm 0.337	0.942 \pm 0.437	0.893 \pm 0.458	0.917 \pm 0.446	0.979 \pm 0.122	0.567 \pm 0.388	0.915 \pm 0.363	0.924 \pm 0.404	0.920 \pm 0.380	0.966 \pm 0.123	0.726 \pm 0.350
Dinov3-B [37]	0.958 \pm 0.431	0.942 \pm 0.450	0.950 \pm 0.441	0.993 \pm 0.097	0.629 \pm 0.354	0.936 \pm 0.349	0.920 \pm 0.327	0.928 \pm 0.320	0.987 \pm 0.090	0.650 \pm 0.312	0.934 \pm 0.325	0.931 \pm 0.317	0.933 \pm 0.320	0.978 \pm 0.100	0.763 \pm 0.364
Dinov3-L [37]	0.976 \pm 0.422	0.925 \pm 0.458	0.950 \pm 0.446	0.992 \pm 0.097	0.516 \pm 0.380	0.975 \pm 0.430	0.837 \pm 0.458	0.901 \pm 0.447	0.983 \pm 0.109	0.572 \pm 0.376	0.925 \pm 0.378	0.935 \pm 0.439	0.930 \pm 0.418	0.977 \pm 0.095	0.761 \pm 0.369
Ours	0.963 \pm 0.372	0.960 \pm 0.300	0.961 \pm 0.308	0.995 \pm 0.004	0.977 \pm 0.030	0.940 \pm 0.267	0.948 \pm 0.300	0.944 \pm 0.298	0.986 \pm 0.011	0.896 \pm 0.029	0.949 \pm 0.284	0.960 \pm 0.302	0.954 \pm 0.311	0.986 \pm 0.018	0.903 \pm 0.027

Free-form Image to Report Retrieval															
Method	32 slices					64 slices					128 slices				
	mAP	R@1	R@5	R@10	NDCG@10	mAP	R@1	R@5	R@10	NDCG@10	mAP	R@1	R@5	R@10	NDCG@10
SigLIPv2-L [41]	0.098 \pm 0.015	0.024 \pm 0.015	0.108 \pm 0.024	0.234 \pm 0.037	0.104 \pm 0.024	0.101 \pm 0.028	0.026 \pm 0.027	0.120 \pm 0.048	0.234 \pm 0.059	0.108 \pm 0.037	0.087 \pm 0.016	0.014 \pm 0.016	0.108 \pm 0.035	0.210 \pm 0.034	0.090 \pm 0.017
CT-CLIP [13]	0.115 \pm 0.018	0.040 \pm 0.015	0.140 \pm 0.047	0.262 \pm 0.034	0.124 \pm 0.020	0.127 \pm 0.015	0.022 \pm 0.014	0.188 \pm 0.035	0.308 \pm 0.024	0.147 \pm 0.017	0.113 \pm 0.016	0.026 \pm 0.020	0.156 \pm 0.033	0.282 \pm 0.043	0.127 \pm 0.019
CT-Vocab [13]	0.093 \pm 0.001	0.020 \pm 0.001	0.110 \pm 0.013	0.230 \pm 0.010	0.102 \pm 0.003	0.093 \pm 0.003	0.022 \pm 0.006	0.108 \pm 0.013	0.208 \pm 0.022	0.096 \pm 0.007	0.090 \pm 0.001	0.020 \pm 0.001	0.102 \pm 0.011	0.196 \pm 0.020	0.090 \pm 0.006
CT-LiPro [14]	0.106 \pm 0.013	0.034 \pm 0.009	0.116 \pm 0.025	0.228 \pm 0.042	0.109 \pm 0.020	0.120 \pm 0.013	0.028 \pm 0.013	0.168 \pm 0.013	0.256 \pm 0.039	0.073 \pm 0.015	0.084 \pm 0.011	0.014 \pm 0.013	0.092 \pm 0.020	0.154 \pm 0.027	0.073 \pm 0.015
Dinov3-Clip [10]	0.091 \pm 0.008	0.020 \pm 0.009	0.104 \pm 0.015	0.212 \pm 0.022	0.095 \pm 0.011	0.092 \pm 0.003	0.022 \pm 0.006	0.104 \pm 0.020	0.204 \pm 0.012	0.093 \pm 0.005	0.094 \pm 0.004	0.022 \pm 0.006	0.106 \pm 0.013	0.216 \pm 0.023	0.098 \pm 0.006
Ours	0.641 \pm 0.037	0.508 \pm 0.055	0.804 \pm 0.041	0.908 \pm 0.030	0.700 \pm 0.031	0.646 \pm 0.056	0.490 \pm 0.071	0.864 \pm 0.060	0.942 \pm 0.042	0.715 \pm 0.052	0.638 \pm 0.046	0.498 \pm 0.065	0.808 \pm 0.049	0.912 \pm 0.039	0.704 \pm 0.044

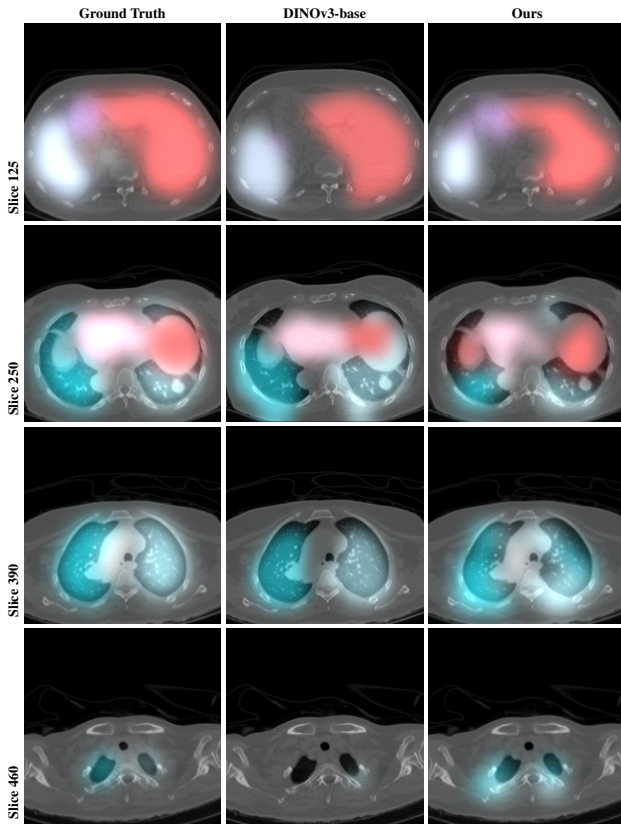


Figure 4. Qualitative comparison of segmentation overlays across four slices (125, 250, 390, 460) in an example volume. Columns correspond to Ground Truth, DINOv3-base, and our method. Rows correspond to different slices, with vertically centered rotated labels for compact visualization.

the block level. In Table 3, the first part evaluates a vision-only setting, where we attach a linear probe to the generated

embeddings and perform 12-organ classification. The second part reports CLIP-style retrieval results, evaluated on the first 50 validation samples from the validation subset.

Chunk-wise downstream tasks are highly relevant for volumetric data, as organs change gradually along the axial axis, so blocks preserve coherent local anatomy and avoid whole-volume label dilution. Supervision is local by nature (patching and organ-wise observations), and aligning it at the block level reduces label leakage and improves feature-label consistency. Fixed-length blocks normalize variable scan lengths, allowing batching. They also enable class rebalancing and hard-example mining while yielding localizable and interpretable outputs. For cross-modal retrieval, text can target the most relevant spatio-temporal neighborhoods, and boundary uncertainty is mitigated by overlapping chunks with consistency and multi-shot supervision.

In Table 3 Classification (Linear Probe), we average slice embeddings along the z-axis for the 2D models. DINOv3 achieves good performance, especially when the number of slices is small. However, as the number of slices increases, its performance degrades noticeably, even though the model is applied once per slice. In contrast, our model consistently improves as the number of slices grows, while being applied once per block. This trend indicates that in a true 3D setting, our SigVLP extracts more accurate and spatially consistent information. Averaging 2D features across slices, even for large models such as DINOv3, inevitably loses valuable 3D context when the number of slices increases.

In Table 3 Free-form Image to Report Retrieval, we evaluate the ability of models to perform text-image multimodal alignment at the chunk level. DINOv3-CLIP, which combines OpenCLIP’s text encoder with a lightweight adapter on top of DINOv3, performs well on general natural image datasets (*e.g.*, COCO [27]). However, it struggles in medical imaging scenarios, where spatial and anatomical pre-

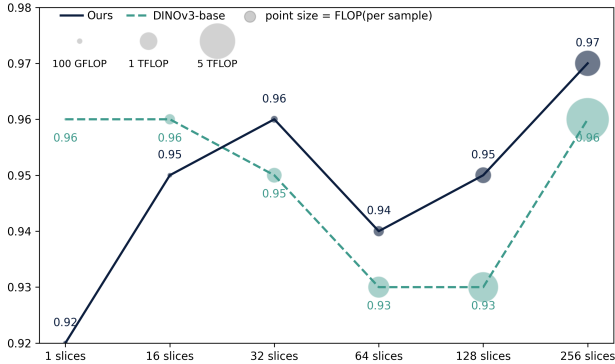


Figure 5. Classification Linear probe F1 score vs. number of slices. Dashed line: DINOv3-Base; solid line: SigVLP; point size shows required floating-point operations (FLOP).

cision are crucial. CT-CLIP, a domain-specific CLIP variant, performs better when the input volume is close to the full-volume setting it was trained on (e.g., 128 slices). In both cases, our model demonstrates a substantial advantage. While CT-CLIP attempts to capture the global semantics of the entire CT volume, our model goes further — it understands where each part belongs and what it represents.

5. Ablation Study

We present ablations exploring different configurations, including variations in RoPE parameter b (which controls the positional rotation frequency in embedding space), different numbers of input slices, and various model training stages. **Input Slice Count Variation.** To explore the limits of our model’s 3D-focused architecture, we evaluate its performance on a 2D image benchmark. Due to architectural constraints, we rely on slice-repetition to fill-in the 16-slice patch-encoder’s input. Results are shown in Fig. 5. We observe that even with a single image as input, our model achieves 92% F1 score, beating many of the baselines shown in Table 3 at other slice counts. Nonetheless, the F1 score is clearly lower in the extreme 1-slice case, compared to the 16-slices to 256-slices results. Additionally, we compared our model to DINOv3-base (second best model in Table 3 after ours). We observe that, DINOv3-base has a clear advantage when evaluated on a single slice, but that advantage quickly disappears as the number of slices increases. This is despite the fact that DINOv3-base is evaluated once per slice, and the results are ensembled, giving it a clear advantage over our model which is only ran once per block of slices.

Variation of Rotary Embedding default in evaluation. During training, we set $b_1 = 1000$. While the default b for RoPE in video transformers is typically 10000, our data chunks are relatively short and of moderate resolution (i.e.,

256 resolution/16 patch size \times 128 slices/16 patch size = 2048 embeddings). Using $b = 10000$ would result in excessively low-frequency positional encoding, leaving much of the representational range underutilized. Therefore, setting $b_1 = 1000$ better matches our spatio-temporal scale.

In this evaluation, we examine the effect of different b values. Although these settings are only changed at inference, we are interested in how RoPE frequency scaling influences performance. As shown in Table 4, smaller b values yield slightly better results. This can be attributed to their ability to preserve higher-frequency variations and maintain finer spatio-temporal structure within short-range context.

Table 4. Performance of SigVLP’s report-to-volume retrieval across slice counts and b values with max. rank 100.

b	R@5 \uparrow	R@10 \uparrow	R@50 \uparrow	MeanRank \downarrow
$0.5b_1$	0.399 ± 0.049	0.547 ± 0.037	0.915 ± 0.026	16.69 ± 1.70
b_1	0.636 ± 0.050	0.769 ± 0.036	0.978 ± 0.010	8.23 ± 0.947
$2b_1$	0.351 ± 0.052	0.480 ± 0.048	0.899 ± 0.025	19.44 ± 1.85

Retrieval experiments across different input slice counts and model training stages.

In Fig. 6, we present the retrieval heatmaps of 50 text-image pairs from the validation subset while changing the model training stage and input slice counts. The diagonal entries correspond to the ground-truth alignments. As model training progresses, high-similarity scores become more concentrated along the diagonal with fewer off-diagonal activations, yielding a cleaner and more distinct alignment pattern. This indicates that, with more training the ambiguity decreases, achieving higher precision cross-modal matching. For our final model, the diagonal concentration is the most pronounced.

6. Conclusion

We have introduced SigVLP, a volumetric vision-language pretraining approach that removes the fixed-depth constraint of conventional 3D architectures by integrating RoPE directly into the attention mechanism. This enables flexible handling of variable-length CT volumes while preserving anatomical continuity and local spatial semantics. By coupling volumetric chunk-wise sampling with organ-aware textual alignment, SigVLP achieves fine-grained visual-textual correspondence and robust generalization across heterogeneous datasets. Our evaluation demonstrates consistent gains over strong baselines such as DINOv3 and CT-CLIP with pronounced improvements in localized, block-wise evaluation. Our findings suggest that adaptive positional encoding and localized supervision can form a scalable foundation for volumetric vision-language models enabling foundation models that jointly reason over anatomy and language. Source code and pretrained weights will be released on GitHub and Hugging Face by the time of the conference.

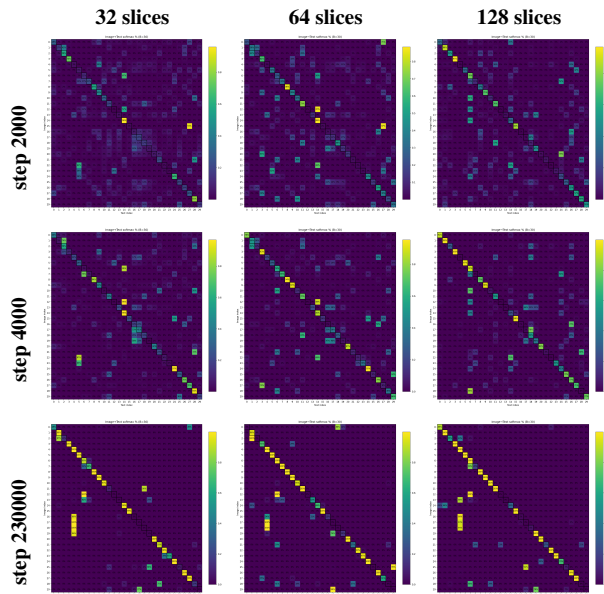


Figure 6. Retrieval of 50 paired samples across model sizes.

References

- [1] Gorkem Can Ates, Yu Xin, Kuang Gong, and Wei Shao. Dc-former: Efficient 3d vision-language modeling with decomposed convolutions. *arXiv preprint arXiv:2502.05091*, 2025. 3, 4
- [2] Jinze Bai, Shuai Bai, Yunfei Chu, Zeyu Cui, Kai Dang, Xiaodong Deng, Yang Fan, Wenbin Ge, Yu Han, Fei Huang, et al. Qwen technical report. *arXiv preprint arXiv:2309.16609*, 2023. 3, 4
- [3] Spyridon Bakas, Hamed Akbari, Aristeidis Sotiras, Michel Bilello, Matthew Rozycki, Justin S. Kirby, John B. Freymann, Keyvan Farahani, and Christos Davatzikos. Advancing The Cancer Genome Atlas Glioma MRI Collections with Expert Segmentation Labels and Radiomic Features. *Sci. Data*, 4:170117, 2017. 2
- [4] Patrick Bilic, Philipp F. Christ, Eugene Vorontsov, Grzegorz Chlebus, Hao Chen, Qi Dou, Chi-Tung Fu, Xiaohong Han, Pheng-Ann Heng, Jürgen Hesser, et al. The Liver Tumor Segmentation Benchmark (LiTS). *arXiv preprint arXiv:1901.04056*, 2019. 2
- [5] Louis Blankemeier, Joseph Paul Cohen, Ashwin Kumar, Dave Van Veen, Syed Jamal Safdar Gardezi, Magdalini Paschali, Zhihong Chen, Jean-Benoît Delbrouck, Eduardo Reis, Cesar Truys, et al. Merlin: A Vision Language Foundation Model for 3D Computed Tomography. *arXiv preprint arXiv:2406.06512*, 2024. 4
- [6] Benedikt Boecking, Naoto Usuyama, Shruthi Bannur, Daniel C. Castro, Anton Schwaighofer, Stephanie Hyland, Marc Wetscherek, Tristan Naumann, Aditya Nori, Jorge Alvarez-Valle, Hoifung Poon, and Ozan Oktay. Making the Most of Text Semantics to Improve Biomedical Vision-Language Processing. In *Lecture Notes in Computer Science (LNCS)*, pages 1–21. Springer, 2022. 3
- [7] Wenting Chen, Linlin Shen, Jingyang Lin, Jiebo Luo, Xiang Li, and Yixuan Yuan. Fine-Grained Image-Text Alignment in Medical Imaging Enables Explainable Cyclic Image-Report Generation. *arXiv preprint arXiv:2312.08078*, 2023. 3
- [8] Yinda Chen, Che Liu, Xiaoyu Liu, Rossella Arcucci, and Zhiwei Xiong. Bimcv-r: A landmark dataset for 3d ct text-image retrieval. In *International Conference on Medical Image Computing and Computer-Assisted Intervention*, pages 124–134. Springer, 2024. 4
- [9] Zhihong Chen, Shizhe Diao, Benyou Wang, Guanbin Li, and Xiang Wan. Towards Unifying Medical Vision-and-Language Pre-Training via Soft Prompts. In *ICCV*, pages 23403–23413, 2023. 4
- [10] duriantaco. dinov3clip: Caption-free adapter that maps dinov3 image embeddings into clip space. <https://github.com/duriantaco/dinov3clip>, 2025. 5, 7, 4
- [11] Mingze Gao, Jingyu Liu, Mingda Li, Jiangtao Xie, Qingbin Liu, Bo Zhao, Xi Chen, and Hui Xiong. TC-LLaVA: Rethinking the Transfer from Image to Video Understanding with Temporal Considerations. *arXiv preprint arXiv:2409.03206*, 2024. 3
- [12] D. Guo, D. Yang, H. Zhang, et al. Deepseek-r1 incentivizes reasoning in llms through reinforcement learning. *Nature*, 645:633–638, 2025. 4
- [13] Ibrahim Ethem Hamamci, Sezgin Er, Furkan Almas, Ayse Gulnihani Simsek, Seval Nil Esirgun, Irem Dogan, Muhammed Furkan Dasdelen, Omer Faruk Durugol, Bastian Wittmann, Tamaz Amiranashvili, Enis Simsar, Mehmet Simsar, Emine Bensus Erdemir, Abdullah Alanbay, Anjany Sekuboyina, Berkan Lafci, Christian Bluethgen, Mehmet Kemal Ozdemir, and Bjoern Menze. Developing Generalist Foundation Models from a Multimodal Dataset for 3D Computed Tomography. *in press Nature Biomedical Engineering*, *arXiv preprint arXiv:2403.17834*, 2024. 2, 4, 5, 6, 7
- [14] Ibrahim Ethem Hamamci, Sezgin Er, Furkan Almas, Ayse Gulnihani Simsek, Seval Nil Esirgun, Irem Dogan, Muhammed Furkan Dasdelen, Bastian Wittmann, Enis Simsar, Mehmet Simsar, et al. A foundation model utilizing chest ct volumes and radiology reports for supervised-level zero-shot detection of abnormalities. *CoRR*, 2024. 5, 7
- [15] Ibrahim Ethem Hamamci, Sezgin Er, and Bjoern Menze. CT2Rep: Automated Radiology Report Generation for 3D Medical Imaging. In *MICCAI*, pages 476–486. Springer, 2024. 2
- [16] Ibrahim Ethem Hamamci, Sezgin Er, Anjany Sekuboyina, Enis Simsar, Alperen Tezcan, Ayse Gulnihani Simsek, Seval Nil Esirgun, Furkan Almas, Irem Dogan, Muhammed Furkan Dasdelen, et al. GenerateCT: Text-Conditional Generation of 3D Chest CT Volumes. In *ECCV*, pages 126–143. Springer, 2024. 2
- [17] Kai Han, Yunhe Wang, Hanting Chen, Xinghao Chen, Jianyuan Guo, Zhenhua Liu, Yehui Tang, An Xiao, Chunjing Xu, Yixing Xu, et al. A survey on vision transformer. *IEEE transactions on pattern analysis and machine intelligence*, 45(1):87–110, 2022. 3

- [18] Nicholas Heller, Niranjan Sathianathen, Arveen Kalapara, Edward Walczak, Keenan Moore, Heather Kaluzniak, Joel Rosenberg, Paul Blake, Zachary Rengel, Makinna Oestreich, Joshua Dean, Michael Tradewell, Aneri Shah, Resha Tejapaul, Zachary Edgerton, Matthew Peterson, Shaneabas Raza, Subodh Regmi, Nikolaos Papanikolopoulos, and Christopher Weight. The KiTS19 Challenge Data: 300 Kidney Tumor Cases with Clinical Context, CT Semantic Segmentations, and Surgical Outcomes. *arXiv preprint arXiv:1904.00445*, 2020. 2
- [19] Zachary Huemann, Samuel Church, Joshua D Warner, Daniel Tran, Xin Tie, Alan B McMillan, Junjie Hu, Steve Y Cho, Meghan Lubner, and Tyler J Bradshaw. Vision-language modeling in pet/ct for visual grounding of positive findings. *arXiv preprint arXiv:2502.00528*, 2025. 4
- [20] Alistair EW Johnson, Tom J Pollard, Seth J Berkowitz, Nathaniel R Greenbaum, Matthew P Lungren, Chih-ying Deng, Roger G Mark, and Steven Horng. Mimic-cxr, a de-identified publicly available database of chest radiographs with free-text reports. *Scientific data*, 6(1):317, 2019. 2
- [21] Keller Jordan, Yuchen Jin, Vlado Boza, Jiacheng You, Franz Cesista, Laker Newhouse, and Jeremy Bernstein. Muon: An Optimizer for Hidden Layers in Neural Networks. <https://kellerjordan.github.io/posts/muon/>, 2024. 3, 1
- [22] Amirhossein Kazemnejad, Inkit Padhi, Karthikeyan Natesan Ramamurthy, Payel Das, and Siva Reddy. The Impact of Positional Encoding on Length Generalization in Transformers. *arXiv preprint arXiv:2305.19466*, 2023. 3
- [23] Changsun Lee, Sangjoon Park, Cheong-Il Shin, Woo Hee Choi, Hyun Jeong Park, Jeong Eun Lee, and Jong Chul Ye. Read like a radiologist: Efficient vision-language model for 3d medical imaging interpretation. *arXiv preprint arXiv:2412.13558*, 2024. 3, 4
- [24] Junnan Li, Ramprasaath Selvaraju, Akhilesh Gotmare, Shafiq Joty, Caiming Xiong, and Steven Chu Hong Hoi. Align before Fuse: Vision and Language Representation Learning with Momentum Distillation. In *NeurIPS*, pages 9694–9705, 2021. 2
- [25] Junnan Li, Dongxu Li, Caiming Xiong, and Steven C.H. Hoi. BLIP: Bootstrapping Language-Image Pre-training for Unified Vision-Language Understanding and Generation. In *ICML*, pages 12888–12900. PMLR, 2022. 2
- [26] Jingyang Lin, Yingda Xia, Jianpeng Zhang, Ke Yan, Le Lu, Jiebo Luo, and Ling Zhang. Ct-glip: 3d grounded language-image pretraining with ct scans and radiology reports for full-body scenarios. *arXiv preprint arXiv:2404.15272*, 2024. 4
- [27] Tsung-Yi Lin, Michael Maire, Serge Belongie, James Hays, Pietro Perona, Deva Ramanan, Piotr Dollár, and C Lawrence Zitnick. Microsoft coco: Common objects in context. In *European conference on computer vision*, pages 740–755. Springer, 2014. 7
- [28] Che Liu, Cheng Ouyang, Yinda Chen, Cesar César Quilodrán-Casas, Lei Ma, Jie Fu, Yike Guo, Anand Shah, Wenjia Bai, and Rossella Arcucci. T3d: Towards 3d medical image understanding through vision-language pre-training. *arXiv preprint arXiv:2312.01529*, 2023. 2, 4
- [29] Che Liu, Sibao Cheng, Miaoqing Shi, Anand Shah, Wenjia Bai, and Rossella Arcucci. IMITATE: Clinical Prior Guided Hierarchical Vision-Language Pre-Training. *arXiv preprint arXiv:2310.07355*, 2024. 3
- [30] Jingyuan Liu, Jianlin Su, Xingcheng Yao, Zhejun Jiang, Guokun Lai, Yulun Du, Yidao Qin, Weixin Xu, Enzhe Lu, Junjie Yan, Yanru Chen, Huabin Zheng, Yibo Liu, Shaowei Liu, Bohong Yin, Weiran He, Han Zhu, Yuzhi Wang, Jianzhou Wang, Mengnan Dong, Zheng Zhang, Yongsheng Kang, Hao Zhang, Xinran Xu, Yutao Zhang, Yuxin Wu, Xinyu Zhou, and Zhilin Yang. Muon is Scalable for LLM Training. *arXiv preprint arXiv:2502.16982*, 2025. 3
- [31] Xindian Ma, Wenyuan Liu, Peng Zhang, and Nan Xu. 3d-rpe: Enhancing long-context modeling through 3d rotary position encoding. In *Proceedings of the AAAI Conference on Artificial Intelligence*, pages 24804–24811, 2025. 3
- [32] Leland McInnes, John Healy, and James Melville. Umap: Uniform manifold approximation and projection for dimension reduction. *arXiv preprint arXiv:1802.03426*, 2018. 5, 6
- [33] OpenAI. Chatgpt-5. <https://chat.openai.com/>, 2025. Large language model by OpenAI. 4
- [34] Alec Radford, Jong Wook Kim, Chris Hallacy, Aditya Ramesh, Gabriel Goh, Sandhini Agarwal, Girish Sastry, Amanda Askell, Pamela Mishkin, Jack Clark, et al. Learning transferable visual models from natural language supervision. In *International conference on machine learning*, pages 8748–8763. PMLR, 2021. 2
- [35] Hadrien Reynaud, Alberto Gomez, Paul Leeson, Qingjie Meng, and Bernhard Kainz. Echoflow: A foundation model for cardiac ultrasound image and video generation. *arXiv preprint arXiv:2503.22357*, 2025. 3
- [36] Zhongyi Shui, Jianpeng Zhang, Weiwei Cao, Sinuo Wang, Ruizhe Guo, Le Lu, Lin Yang, Xianghua Ye, Tingbo Liang, Qi Zhang, and Ling Zhang. Large-scale and Fine-grained Vision-Language Pre-Training for Enhanced CT Image Understanding. *arXiv preprint arXiv:2501.14548*, 2025. 3, 4
- [37] Oriane Siméoni, Huy V. Vo, Maximilian Seitzer, Federico Baldassarre, Maxime Oquab, Cijo Jose, Vasil Khalidov, Marc Szafraniec, Seungeun Yi, Michaël Ramamonjisoa, Francisco Massa, Daniel Haziza, Luca Wehrstedt, Jianyuan Wang, Timothée Darcet, Théo Moutakanni, Leonel Sentana, Claire Roberts, Andrea Vedaldi, Jamie Tolan, John Brandt, Camille Couprie, Julien Mairal, Hervé Jégou, Patrick Labatut, and Piotr Bojanowski. Dinov3. *arXiv preprint arXiv:2508.10104*, 2025. 5, 6, 7
- [38] Jianlin Su, Yu Lu, Shengfeng Pan, Ahmed Murtadha, Bo Wen, and Yunfeng Liu. RoFormer: Enhanced Transformer with Rotary Position Embedding. *arXiv preprint arXiv:2104.09864*, 2023. 3
- [39] Kimi Team, Yifan Bai, Yiping Bao, Guanduo Chen, Jiahao Chen, Ningxin Chen, Ruijue Chen, Yanru Chen, Yuankun Chen, Yutian Chen, et al. Kimi k2: Open agentic intelligence. *arXiv preprint arXiv:2507.20534*, 2025. 3
- [40] Hugo Touvron, Thibaut Lavril, Gautier Izacard, Xavier Martinet, Marie-Anne Lachaux, Timothée Lacroix, Baptiste Rozière, Naman Goyal, Eric Hambro, Faisal Azhar, et al.

- Llama: Open and efficient foundation language models. *arXiv preprint arXiv:2302.13971*, 2023. 3
- [41] Michael Tschannen, Alexey Gritsenko, Xiao Wang, Muhammad Ferjad Naeem, Ibrahim Alabdulmohsin, Nikhil Parthasarathy, Talfan Evans, Lucas Beyer, Ye Xia, Basil Mustafa, et al. Siglip 2: Multilingual vision-language encoders with improved semantic understanding, localization, and dense features. *arXiv preprint arXiv:2502.14786*, 2025. 3, 5, 6, 7, 4
- [42] Cheng Tung, Yu Lin, Jianfeng Yin, Qi Ye, and Hongming Chen. Exploring Vision Language Pretraining with Knowledge Enhancement via Large Language Model. In *Lecture Notes in Computer Science (LNCS)*. Springer, 2024. 3
- [43] Jiayi Wang, Hadrien Reynaud, Franciskus Xaverius Erick, and Bernhard Kainz. CtfLOW: Video-inspired latent flow matching for 3d ct synthesis. In *Proceedings of the IEEE/CVF International Conference on Computer Vision*, pages 6750–6758, 2025. 3
- [44] Peng Wang, Shuai Bai, Sinan Tan, Shijie Wang, Zhihao Fan, Jinze Bai, Keqin Chen, Xuejing Liu, Jialin Wang, Wenbin Ge, Yang Fan, Kai Dang, Mengfei Du, Xuancheng Ren, Rui Men, Dayiheng Liu, Chang Zhou, Jingren Zhou, and Junyang Lin. Qwen2-VL: Enhancing Vision-Language Model’s Perception of the World at Any Resolution. *arXiv preprint arXiv:2409.12191*, 2024. 3
- [45] Yuli Wang, Yuwei Dai, Craig Jones, Haris Sair, Jinglai Shen, Nicolas Loizou, Wen-Chi Hsu, Maliha Imami, Zhicheng Jiao, Paul Zhang, et al. Enhancing vision-language models for medical imaging: bridging the 3d gap with innovative slice selection. *Advances in Neural Information Processing Systems*, 37:99947–99964, 2024. 2
- [46] Zifeng Wang, Zhenbang Wu, Dinesh Agarwal, and Jimeng Sun. MedCLIP: Contrastive Learning from Unpaired Medical Images and Text. In *Proc. Conf. Empirical Methods in Natural Language Processing (EMNLP)*, pages 3876–3887, Abu Dhabi, United Arab Emirates, 2022. Association for Computational Linguistics. 2, 3
- [47] Jakob Wasserthal, Hanns-Christian Breit, Manfred T Meyer, Maurice Pradella, Daniel Hinck, Alexander W Sauter, Tobias Heye, Daniel T Boll, Joshy Cyriac, Shan Yang, et al. Totalsegmentator: robust segmentation of 104 anatomic structures in ct images. *Radiology: Artificial Intelligence*, 5(5): e230024, 2023. 2, 3, 5
- [48] Xilin Wei, Xiaoran Liu, Yuhang Zang, Shengyuan Ding, Xiaoyi Dong, Yuhang Cao, Haodong Duan, Qipeng Guo, Jiaqi Wang, Xipeng Qiu, and Dahua Lin. VideoRoPE++: Towards Better Video Rotary Position Embedding. https://github.com/Wiselnn570/VideoRoPE/blob/main/videorope_plus/VideoRoPE_plus.pdf, 2025. 3
- [49] Xilin Wei, Xiaoran Liu, Yuhang Zang, Xiaoyi Dong, Pan Zhang, Yuhang Cao, Jian Tong, Haodong Duan, Qipeng Guo, Jiaqi Wang, Xipeng Qiu, and Dahua Lin. VideoRoPE: What Makes for Good Video Rotary Position Embedding? *arXiv preprint arXiv:2502.05173*, 2025. 3
- [50] Jian Wu, Xiaohong Zhang, Yicheng Zhang, Yujie Wang, and Weidi Xie. MedKLIP: Medical Knowledge Enhanced Language-Image Pre-Training for X-ray Diagnosis. In *ICCV*, pages 19493–19503, 2023. 3
- [51] Yutong Xie, Qi Chen, Sinuo Wang, Minh-Son To, Iris Lee, Ee Win Khoo, Kerolos Hendy, Daniel Koh, Yong Xia, and Qi Wu. PairAug: What Can Augmented Image-Text Pairs Do for Radiology? In *CVPR*, pages 11652–11657, 2024. 4
- [52] Yu Xin, Gorkem Can Ates, Kuang Gong, and Wei Shao. Med3dvlm: An efficient vision-language model for 3d medical image analysis. *arXiv preprint arXiv:2503.20047*, 2025. 3, 4
- [53] Murong Xu, Tamaz Amiranashvili, Fernando Navarro, Maksym Fritsak, Ibrahim Ethem Hamamci, Suprosanna Shit, Bastian Wittmann, Sezgin Er, Sebastian M Christ, Ezequiel de la Rosa, et al. Cads: A comprehensive anatomical dataset and segmentation for whole-body anatomy in computed tomography. *arXiv preprint arXiv:2507.22953*, 2025. 2, 3
- [54] Bin Yan and Minghui Pei. Clinical-BERT: Vision-Language Pre-training for Radiograph Diagnosis and Reports Generation. In *AAAI*, pages 2982–2990, 2022. 3
- [55] Xiaohua Zhai, Basil Mustafa, Alexander Kolesnikov, and Lucas Beyer. Sigmoid loss for language image pre-training. In *Proceedings of the IEEE/CVF international conference on computer vision*, pages 11975–11986, 2023. 3, 4
- [56] Xiaohong Zhang, Chuang Wu, Yuxuan Zhang, Qiu Jin, Yuxing Tang, Jianglin Duan, Haotian Bai, Dong Xu, Hong-Yu Zhou, Linyuan Sun, et al. Knowledge-Enhanced Visual-Language Pre-Training on Chest Radiology Images. *Nat. Commun.*, 14:4542, 2023. 3
- [57] Yuhao Zhang, Hang Jiang, Yasuhide Miura, Christopher D. Manning, and Curtis P. Langlotz. ConVIRT: Contrastive Learning of Medical Visual Representations from Paired Images and Text. In *Proc. Mach. Learn. Healthc. Conf. (MLHC)*, pages 2–25. PMLR, 2022. 2, 3
- [58] Ziyang Zhang, Yang Yu, Xulei Yang, and Si Yong Yeo. VELVET-Med: Vision and Efficient Language Pre-Training for Volumetric Imaging Tasks in Medicine. *arXiv preprint arXiv:2508.12108*, 2025. 4

SigVLP: Sigmoid Volume-Language Pre-Training for Self-Supervised CT-Volume Adaptive Representation Learning

Supplementary Material

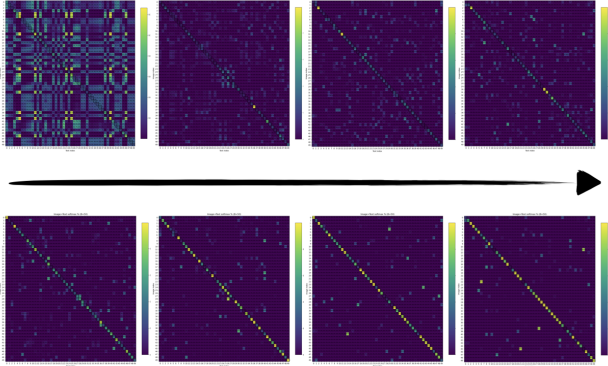


Figure 7. Heatmap Grids of Image-to-Text Retrieval (50-Val Set; Every 500 Steps): Adam in the Upper Row, Muon in the Lower Row

A. Muon Optimizer

We use a single optimizer that applies **Muon** to matrix parameters with two or more dimensions and defaults to AdamW for everything else (*e.g.*, biases, gains, embeddings). In this paper, we directly use the optimizer provided in the GitHub repository from [21]. **Muon update:** For parameter \mathbf{w} with gradient \mathbf{g}_t , step size η , decay λ , and momentum β ,

$$\mathbf{u}_t = \beta \mathbf{u}_{t-1} + (1 - \beta) \mathbf{g}_t, \quad (7)$$

$$\mathbf{w} \leftarrow (1 - \eta\lambda) \mathbf{w} - \eta \mathbf{u}_t. \quad (8)$$

This is a non-adaptive, momentum-only update (no second moment or variance normalization), which we found preferable for large weight matrices. Other parameters use AdamW.

Across both visualizations, Muon consistently outperforms AdamW. In Figure 7, the Muon training curve exhibits lower variance and converges to a more stable loss than AdamW, indicating smoother optimization and reduced gradient noise. Figure 8 further confirms this trend as the retrieval heatmaps under Muon become cleaner and more near-diagonal, while AdamW produces noisier, less structured similarity patterns. Overall, Muon provides improved stability and alignment quality compared with pure AdamW under identical model settings.

B. Feature Visualization

In Section 4 Figure 3, we present UMAP feature visualizations. For completeness, we also evaluate t-SNE pro-

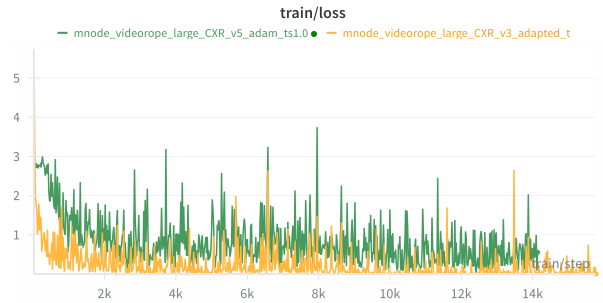


Figure 8. Training Loss vs. Steps — Adam (green) vs. Muon (yellow), Identical Model Configuration

jections across different classes for the same embeddings. The results remain consistent with those in Figure 9: the clusters produced by DINOv3 appear disorganized and randomly clustered, while those from CT-RATE and CT-Vocab exhibit mixed boundaries. In contrast, our model yields smoother and more coherent cluster distribution, showing behavior closely aligned with the class fine-tuned CT-LiPro model.

C. Computational Cost and Throughput Comparison

We report the computational efficiency of our model under different temporal lengths T and compare it against DINOv3. For each setting, we measure the FLOP per sample, average latency, and effective FLOPs computed as $\text{FLOP}/(\text{latency in seconds})$. Note that for our model, $T = 1$ shares the same cost as $T = 16$ due to padding. Results are summarized in Table 5.

Our model demonstrates consistently higher computational efficiency compared with DINOv3. As shown in Table 5, for all temporal lengths $T \geq 32$, our method requires substantially fewer FLOP per sample while achieving comparable or higher throughput. Combined with the accuracy curves in section 5 Fig. 5, it indicates that our model attains better performance using significantly lower computational resources than DINOv3, except when the slice count is extremely small ($T < 16$).

D. Comparison of Padding Strategies

In Section 5, we analyze the effect of input slice count variation. Because our patch size along the z-axis is fixed to 16,

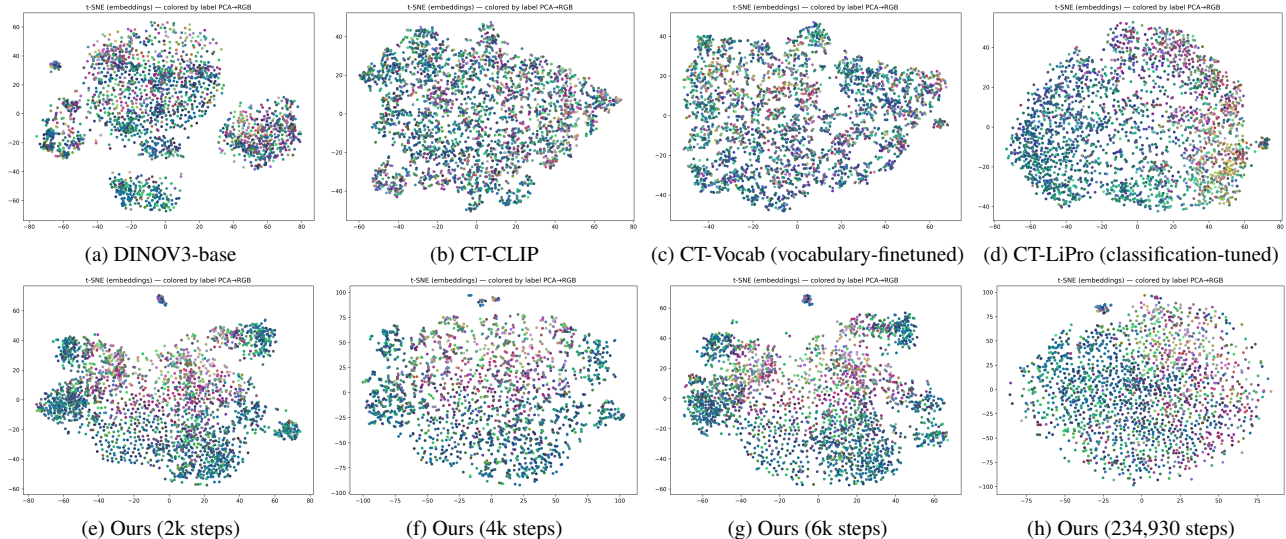


Figure 9. **t-SNE of evaluation embeddings** across baselines and our model. Colors denote abnormality classes (similar hues indicate semantically related labels). *Top row*: DINOv3-base, CT-CLIP, CT-Vocab (vocabulary-finetuned), CT-LiPro (classification-finetuned). *Bottom row*: Ours at 2k, 4k, 6k, and 234,930 training steps.

Table 5. Comparison of computational cost and throughput for Ours vs. DINOv3 at different slices number. FLOP/sample corresponds to one forward pass per sample.

Slices Count	Ours			DINOv3		
	FLOP/sample	Latency (ms)	FLOP/s	FLOP/sample	Latency (ms)	FLOP/s
256	2.080 TFLOP	147.692	14.09	5.720 TFLOP	137.422	41.62
128	0.834 TFLOP	53.896	15.47	2.860 TFLOP	69.674	41.04
64	0.365 TFLOP	24.588	14.86	1.430 TFLOP	36.035	39.68
32	0.170 TFLOP	23.010	7.38	0.715 TFLOP	18.440	38.78
16	0.082 TFLOP	22.758	3.59	0.358 TFLOP	9.423	37.93
1	0.082 TFLOP	22.758	3.59	0.022 TFLOP	12.555	1.78

padding is required when evaluating cases with only 1 or 8 slices. We compared “repeat padding” and “zero padding”, and ultimately adopted repeat padding because our quantitative results, presented in Table 6, showed improved performance. In particular, when $slice = 1$, repeat padding yields a substantial improvement, with precision increasing from 0.830 to 0.931.

More detailed per-organ comparisons are visualized in Fig. 10. When $slice = 1$, repeat padding significantly outperforms zero padding across almost all organs. Zero padding performs especially poorly on small or thin structures such as *Right Kidney* (0.051 \rightarrow 0.723), *Left Kidney* (0.147 \rightarrow 0.852), and *Pancreas* (0.397 \rightarrow 0.786), while large organs such as *Spleen* (0.623 \rightarrow 0.833) and *Liver* (0.744 \rightarrow 0.891) also benefit noticeably. Overall, repeat padding consistently achieves higher F1 scores, with the largest gains observed on low-contrast or shape-sensitive organs.

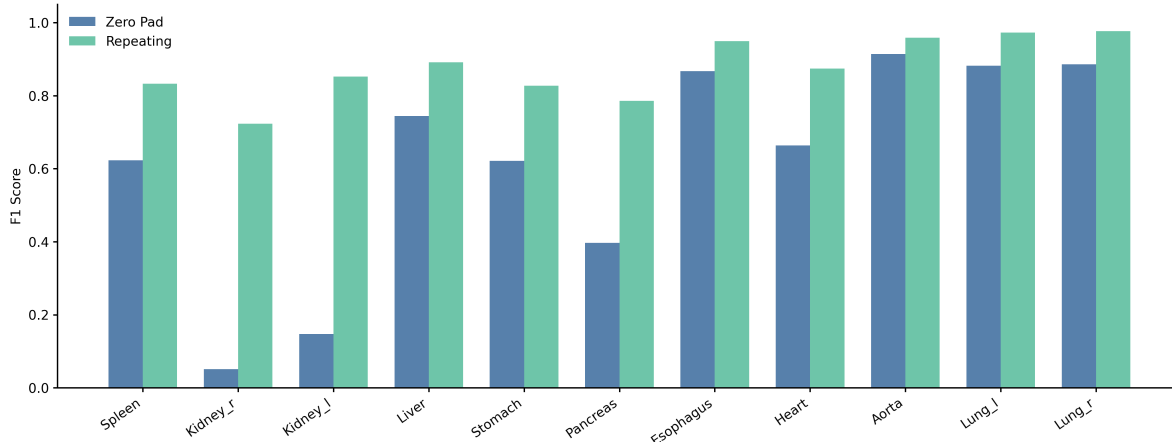
When $slice = 8$, the performance gap narrows, but the trend remains unchanged: repeat padding achieves the best results for nearly every organ, e.g., *Right Kidney*

Table 6. Comparison of padding strategies for different input slice counts.

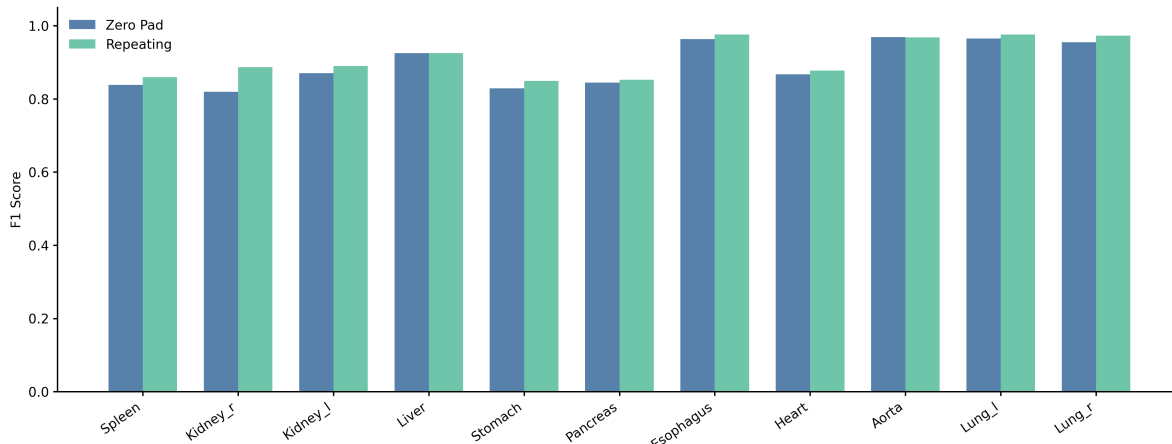
Slices Num.	Pad method	Precision	Recall	F1	AUC	mAP
1	Repeat	0.931	0.906	0.918	0.986	0.936
	Zero Pad	0.830	0.750	0.788	0.922	0.778
8	Repeat	0.951	0.925	0.938	0.990	0.960
	Zero Pad	0.930	0.919	0.925	0.986	0.943

(0.819 \rightarrow 0.887), *Pancreas* (0.844 \rightarrow 0.852), and *Left Lung* (0.965 \rightarrow 0.976). Although the improvements are smaller as there is more contextual information available, repeat padding still provides more stable and accurate predictions overall.

These results demonstrate that our model, which was not trained on empty slices, is sensitive to the content of each individual input slice. Motivated by this conclusion, all downstream components that involve padding likewise employ the repeat strategy to provide as much contextual information as possible to the model.



(a) Per-organ F1 for Slice = 1



(b) Per-organ F1 for Slice = 8

Figure 10. Comparison of Zero Padding and Repeat Padding across organs under different slice counts.

E. 1500 Volumes Report Retrieval

Additionally, in this paper, we evaluate retrieval performance on the full validation set. However, the performance differences among baseline methods on the full set are extremely small, often below 0.001 across several metrics, making it difficult to draw reliable or meaningful conclusions from a single pass evaluation. Therefore, in the main paper we primarily report results based on 100 bootstrap subsets, which provide a more stable, statistically robust, and discriminative comparison across methods. For completeness, the full-set results are included in Table 7 in this appendix. The overall trends are fully consistent with those presented in the paper: our model outperforms all baselines across every retrieval metric. Notably, despite the difficulty of retrieving a 200-slice volume from 1,500 candidates using only a full radiology report, our method achieves a Recall@1 of 0.0998. This is remarkably high for large-scale

radiology-report-to-CT retrieval and substantially exceeds existing state-of-the-art approaches.

F. Organ-wise F1 Performance Across Varying Numbers of Input Slices

To further examine how the amount of input 3D context influences organ-level performance, we visualize the F1 scores of 11 organs across six different slice counts (1, 16, 32, 64, 128, 256). The radar plots in Figure 11 reveal how prediction stability and anatomical completeness improve as more slices become available.

Across all six configurations, the overall trend is consistent with the observations made in Figure 5: When only one slice is provided, the performance distribution is highly uneven, while larger slice counts (64–256) yield more stable, high-magnitude F1 scores across all organs. This confirms that richer 3D context leads to more consistent anatomical

Table 7. **1500 validation subset whole-body retrieval across different CLIP-based methods. For our proposed SigVLP method, we employ reconstructed reports generated through our pipeline.** Retrieval is performed between a 200-slice CT volume and the full radiology report.

Model	R@1	R@5	R@10	R@50	R@100	MeanRank	mAP
SigLIPv2-L[41]	0.002	0.003	0.007	0.033	0.065	751.77	0.006
CT-CLIP[13]	0.007	0.029	0.045	0.161	0.263	378.39	0.024
CT-Vocab[13]	0.001	0.004	0.007	0.035	0.071	729.09	0.006
DINOv3-CLIP[10]	0.001	0.003	0.008	0.030	0.064	751.70	0.006
Ours	0.098	0.251	0.336	0.599	0.730	107.13	0.180

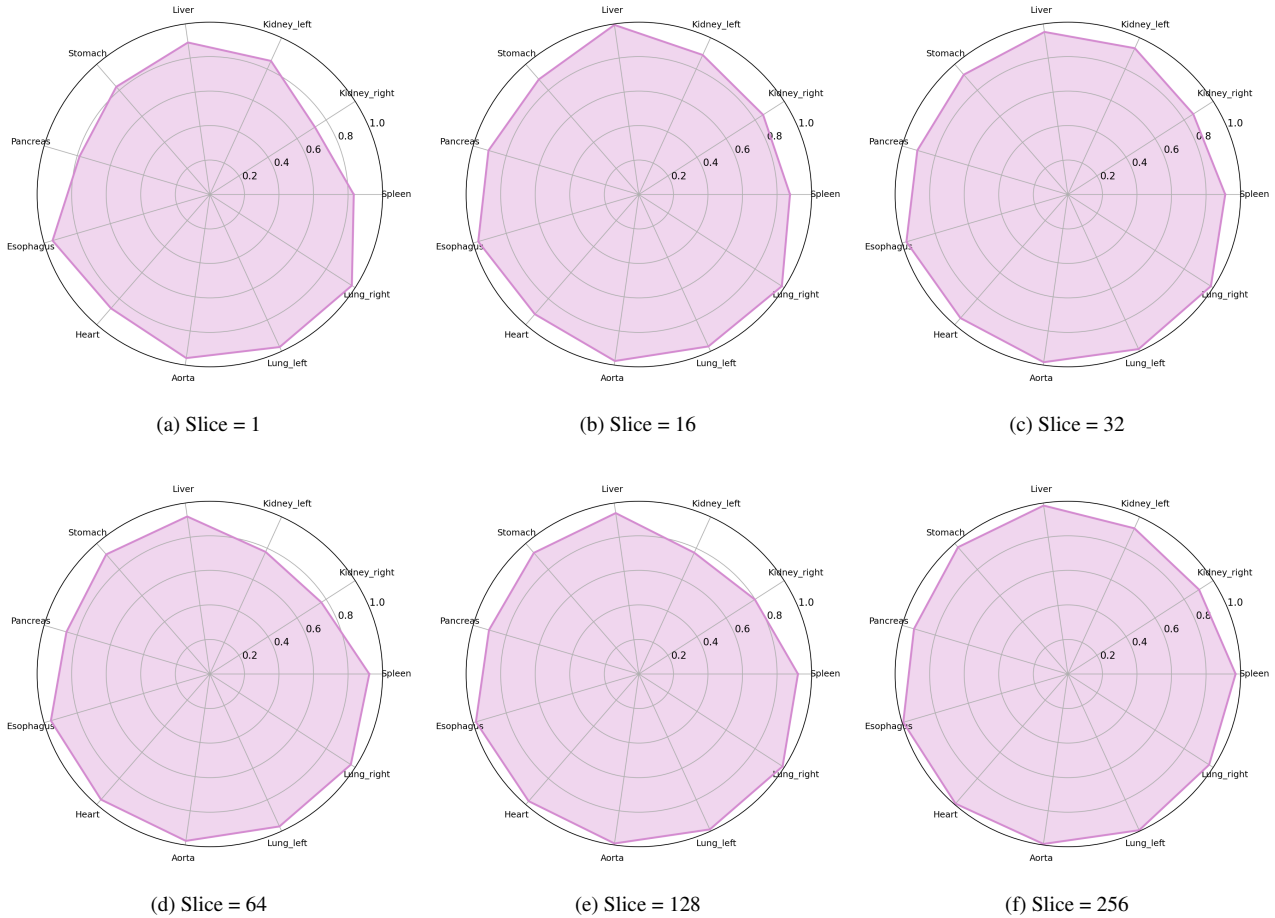


Figure 11. Organ-wise F1 radar plots across different numbers of input slices.

reasoning and improved multi-organ segmentation performance.

G. Structured Annotation

To improve alignment between free-text radiology descriptions and our model’s structured prediction space, we employed GPT-5 Mini to convert the original free-text reports into standardized organ-level annotations. The LLM maps each mentioned anatomical region into a predefined schema, and leverages categorical status labels (*e.g.*, nor-

mal, abnormal, not examined) along with corresponding summarized findings. In clinical practice, the label *not examined* implicitly suggests that the corresponding organ is generally considered healthy unless otherwise indicated.

train.7.a.1.json

```
"Adrenal gland": { "status": "normal", "findings": "Bilateral adrenal gland calibration was normal and no space-occupying lesion was detected." },
"Aorta": { "status": "normal", "findings": "No dilatation was detected in the thoracic aorta; calibration of thoracic main vascular structures is natural." },
"Brain": { "status": "not_examined", "findings": "not_examined" },
"Breast": { "status": "not_examined", "findings": "not_examined" },
"Clavicle": { "status": "not_examined", "findings": "not_examined" },
"Colon": { "status": "not_examined", "findings": "not_examined" },
"Esophagus": { "status": "normal", "findings": "Thoracic esophagus calibration was normal and no significant pathological wall thickening was detected." },
"Femur": { "status": "not_examined", "findings": "not_examined" },
"Gallbladder": { "status": "not_examined", "findings": "not_examined" },
"Gluteus muscles": { "status": "not_examined", "findings": "not_examined" },
"Great vessels": { "status": "normal", "findings": "Calibration of thoracic main vascular structures is natural; no dilatation of the thoracic aorta." },
"Heart": { "status": "normal", "findings": "Heart contour size is natural; pericardial thickening-effusion was not detected." },
"Hip/Pelvis": { "status": "not_examined", "findings": "not_examined" },
"Humerus": { "status": "not_examined", "findings": "not_examined" },
"Iliopsoas": { "status": "not_examined", "findings": "not_examined" },
"Inferior vena cava": { "status": "not_examined", "findings": "not_examined" },
"Kidney": { "status": "not_examined", "findings": "not_examined" },
"Liver": { "status": "abnormal", "findings": "Liver size increased (hepatomegaly). Other upper abdominal sections within the examination area are normal." },
"Lung": { "status": "abnormal", "findings": "Pleuroparenchymal sequelae increase in density and paracicatricial bronchiectasis in the right upper lobe; increased pleuroparenchymal sequelae density in the left lower lobe; calcified nonspecific parenchymal nodules 3{3.5 mm in both lungs; no pleural effusion." },
"Lymph nodes": { "status": "abnormal", "findings": "A few calcified lymph nodes/nodules (3.5 mm left middle lobe, 3 mm right upper lobe); no pathological mediastinal/hilar lymphadenopathy." },
"Pancreas": { "status": "not_examined", "findings": "not_examined" },
"Paraspinal muscles": { "status": "not_examined", "findings": "not_examined" },
"Pericardium": { "status": "normal", "findings": "Pericardial thickening-effusion was not detected." },
"Pleura": { "status": "normal", "findings": "Bilateral pleural thickening-effusion was not detected." },
"Portal vein and splenic vein": { "status": "not_examined", "findings": "not_examined" },
"Prostate": { "status": "not_examined", "findings": "not_examined" },
"Pulmonary vessels": { "status": "not_examined", "findings": "not_examined" },
"Ribs": { "status": "not_examined", "findings": "not_examined" },
"Scapula": { "status": "not_examined", "findings": "not_examined" },
"Skull": { "status": "not_examined", "findings": "not_examined" },
"Small intestine": { "status": "not_examined", "findings": "not_examined" },
"Spinal cord": { "status": "not_examined", "findings": "not_examined" },
"Spine/Vertebrae": { "status": "normal", "findings": "No lytic-destructive lesion was detected in bone structures." },
"Spleen": { "status": "not_examined", "findings": "not_examined" },
"Sternum": { "status": "not_examined", "findings": "not_examined" },
"Stomach": { "status": "not_examined", "findings": "not_examined" },
```

```
"Thyroid gland": { "status": "not_examined", "findings": "not_examined" },
"Trachea": { "status": "normal", "findings": "Trachea and both main bronchi are
open; no occlusive pathology was detected." },
"Urinary bladder": { "status": "not_examined", "findings": "not_examined" },
"general": "Mediastinal structures were evaluated as suboptimal since the examination
was unenhanced; an intravascular catheter projects superiorly to the vena cava."
}
```